Multiple jets and bursting in the rapidly rotating convecting two-dimensional annulus model with nearly plane-parallel boundaries

By JON ROTVIG[1] AND CHRIS A. JONES[2]

[1]Max-Planck-Institute for Solar System Research, 37191 Katlenburg-Lindau, Germany
[2]Department of Applied Mathematics, University of Leeds, Leeds LS2 9JT, UK

We analyse numerical solutions in the annulus model of rotating convection outside the tangent cylinder in a spherical shell. This model is capable of producing zonal flows with multiple jets. We investigate the conditions under which multi-jet solutions can be found. Although boundary friction reduces the strength of the zonal flow, it enhances the formation of multi-jets. More general models have a well-defined Ekman-layer term. In the annulus model, the Ekman-layer term has a similar form, but with variable strength. We have explored how the strength of the Ekman-layer term affects the form and strength of the zonal flows. We find that strong multi-jet zonal flows can be found for realistic values of the boundary friction, and hence have implications for convection in experiments and enclosed planetary cores. In addition, at higher Rayleigh numbers the importance of boundary friction is enhanced relative to bulk viscosity. Convection in the annulus model often occurs in the form of short-lived bursts as opposed to quasi-steady equilibriums. We have investigated when these events occur and their characteristics. In particular, we find precursors and afterglows of the convective bursts. We have obtained the β-scaling for a range of quantities when the thermal forcing is moderate. An examination of the components of the energy rate of change shows that the total Ekman-layer dissipation is of second order in the large β limit. However, the β-scaling of the forces driving the zonal flow seems to suggest that the zonal Ekman-layer dissipation remains important. We have introduced the concept of flow Taylorization, an analogue to the Taylorization used in magnetohydrodynamics studies and find a β-scaling of this quantity compatible with the moderate strength of the zonal flow. We also determine the typical length scale on which convection operates and compare this to the numerically determined length scale.

1. Introduction

The study of thermal convection in rotating spherical shells has applications in meteorology, oceanography and planetary science. Large zonal flows are observed in the atmospheres of the outer planets, and differential rotation is observed in the Sun and is likely in other stars. All these phenomena are believed to be driven by the interaction of convection and rotation. Although convection in planetary cores may be affected by magnetic fields, an understanding of the non-magnetic problem is useful for understanding planetary dynamos.

In these problems, a key issue is the predicting of the form and strength of the differential rotation. In the solar case, this can be tested against helioseismology

results. This work has been reviewed by Toomre (2003) and Elliott (2003). Another outstanding problem is the formation of multi-jets as observed in Jupiter's atmosphere, where a zonal flow with alternating direction provides a banded system of jets that extends over the whole planet (Limaye 1986; Porco *et al.* 2003). These azimuthal winds are much stronger than the radial convection.

The interior of Jupiter is believed to consist of a core of metallic hydrogen with a radius of around 55 000 km, surrounded by an envelope of molecular hydrogen and helium, approximately 15 000 km deep. Scale analysis of conditions in the core (Starchenko & Jones 2002; Jones 2003) and observations of the magnetic field of Jupiter (Russell, Yu & Kivelson 2003) suggest that the flow in the core is very slow compared to the zonal flow observed at the surface. It remains an open problem whether the zonal flows are confined to a thin layer in the top few hundred kilometres of the planet or extend deep into the interior as suggested by Busse (1976). This controversy has been reviewed by Yano (1998).

Nonlinear three-dimensional simulations of rotating convection in spherical shells were pioneered by Gilman (1977, 1978*a, b*). Although he analyses slowly rotating systems, as appropriate to the Sun, he finds significant influence of the Coriolis force when the driving is not too large. Zhang (1992) considers rapidly rotating shells. These simulations are at the onset of convection, and also reach to weakly nonlinear solutions. In the latter case, he explores zonal flow generation by Reynolds stresses. More work on rapidly rotating shells has been performed by Tilgner & Busse (1997), Grote & Busse (2001), Christensen (2001, 2002), and Busse (2002), exploiting the improvements in computational resources. In particular, it is found that strong zonal flows may be generated, being either approximately steady or strongly oscillatory. These latter oscillations are caused by regular bursts of convection (Grote & Busse 2001), which we will investigate further in this paper.

Three-dimensional numerical simulations are numerically very expensive and in general they have problems reaching the small viscous dissipation levels that apply in many planetary convection problems. An important alternative to numerical simulations are laboratory experiments exploring convection in rapidly rotating systems (Busse & Carrigan 1976; Manneville & Olson 1996; Aubert *et al.* 2001). In these experiments, centrifugal acceleration replaces acceleration due to gravity. The fluid is cooled at an inner sphere (or cylinder) to drive convection. These systems allow a low ratio between the viscous force and the Coriolis force.

Several models take advantage of the strong Coriolis force which tends to reduce the dependence on the coordinate along the rotation axis, thus making the problem quasi-two-dimensional. The annulus model developed in Busse (1970) exploits this fact. Also the models in Aubert, Gillet & Cardin (2003), Gillet & Jones (2006) and Rotvig (2006) belong to this family of quasi-geostrophic models. They show that their models in many respects compare well with corresponding three-dimensional results in the region outside the tangent cylinder. In shallow-layer models, two-dimensionality is enforced by the strong density stratification in the surface layers. This model type has been simplified further by forcing a turbulent input at small wavelength and studying the subsequent time-dependent evolution (Cho & Polvani 1996; Yano, Talagrand & Drossart 2005).

The present paper is based on the annulus model. Being a simplified model, it has, of course, some shortcomings. One such is the lack of density variations as observed in giant gas planets. When the Rossby and Ekman numbers are small, and the driving is not too large, we still expect convection to be largely independent of the coordinate along the rotation axis. However, compressibility affects vorticity generation and the
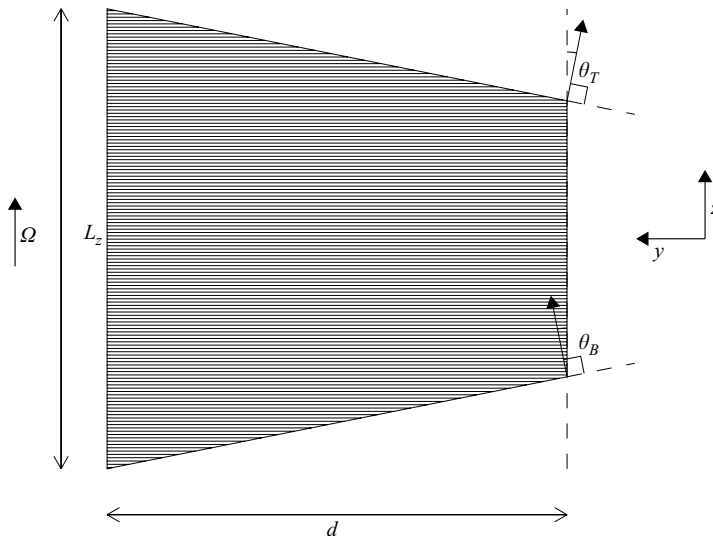
FIGURE 1. The duct geometry. The angle of inclination $\theta_T > 0$ and $\theta_B < 0$.

β-parameter (Evonuk & Glatzmaier 2004; Ingersoll & Pollard 1982). In Brummell & Hart (1993) and Jones, Rotvig & Abdulrahman (2003, hereinafter referred to as JRA), it is shown that the annulus model is able to produce strong zonal flows with a few jets. Also the convection bursts occur. However, as shown in JRA, multi-jet behaviour begins to occur when the ratio of the viscous force to the Coriolis force is sufficiently small. In this paper we study these phenomena extensively.

This paper is organized as follows. We define the model set-up in §2. In §3, we consider the results of a large number of numerical simulations, determining the Ekman-layer strengths at which multi-jet solutions occur. In §4, we investigate the bursting phenomenon, showing that precursors and afterglow effects are present, and analyse some waves excited by the bursts. We study the components of the energy fluctuations and the balances in the zonal flow equation. In §5, we introduce the concept of flow Taylorization and find its β-scaling. Finally, in §6, we derive the convection length scale and compare this to the numerical results.

2. The model

We consider a rotating and incompressible fluid contained in a periodic duct of length L_x along the x-axis (figure 1). The duct has vertical sidewalls and tilted top and bottom boundaries. The angle of inclination of the latter boundaries are θ_T and θ_B, respectively, measured clockwise from e_z. The angular velocity $\boldsymbol{\Omega}$ is along the z-axis. We choose the uniform gravity g in the y-direction. The x- and y-directions correspond to the azimuthal and opposite radial directions in spherical geometry. The convection problem in the Boussinesq approximation is then given by

$$E\left(\frac{\partial \boldsymbol{u}}{\partial t} + \boldsymbol{u} \cdot \nabla \boldsymbol{u}\right) + 2\boldsymbol{e}_z \times \boldsymbol{u} = -\nabla P - Ra'T\boldsymbol{e}_y + E\nabla^2\boldsymbol{u}, \qquad (2.1a)$$

$$\frac{\partial T}{\partial t} + \boldsymbol{u} \cdot \nabla T = \frac{1}{Pr}\nabla^2 T, \qquad (2.1b)$$

$$\nabla \cdot \boldsymbol{u} = 0. \qquad (2.1c)$$

The pressure P includes the centrifugal potential. The length scales are taken as in the spherical dynamo benchmark (Christensen *et al.* 2001),

$$r : d, \quad t : d^2/\nu, \quad \boldsymbol{u} : \nu/d, \quad P : \rho\nu\Omega, \quad T : \Delta T, \tag{2.2}$$

where (ν, ρ) is the kinematic viscosity and density. The system is heated at the inner boundary and ΔT denotes the temperature difference between the inner and outer wall. The Rayleigh, Ekman and Prandtl numbers are

$$Ra' = \frac{\alpha g \Delta T d}{\nu\Omega}, \quad E = \frac{\nu}{\Omega d^2}, \quad Pr = \frac{\nu}{\kappa}. \tag{2.3}$$

Here, α is the thermal expansion coefficient at constant pressure, and κ is the thermal diffusivity. We will decompose the temperature $\widetilde{T} + \hat{T}$ into a basic state profile $\widetilde{T}$ with no heat sources, $\nabla^2\widetilde{T} = 0$, and a perturbation $\hat{T}$. The temperature perturbation $\hat{T}$ is zero at the boundaries. Stress-free boundaries are imposed at the vertical walls, and non-slip boundary conditions at the top and bottom surface. The Ekman layers at the non-slip boundaries are described in Greenspan (1968). At a boundary point, the perpendicular, inward directed, unit vector is denoted by $\boldsymbol{e}_n$. The normal component of the Ekman suction $\boldsymbol{u}_E$ may then be written as

$$\boldsymbol{e}_n \cdot \boldsymbol{u}_E = \frac{E^{1/2}}{2} \boldsymbol{e}_n \cdot \nabla \times \left\{ \frac{1}{\sqrt{|\boldsymbol{e}_n \cdot \boldsymbol{e}_z|}} \left[\boldsymbol{e}_n \times \boldsymbol{u} + \text{sign}(\boldsymbol{e}_n \cdot \boldsymbol{e}_z)\boldsymbol{u} \right] \right\}. \tag{2.4}$$

In the two-dimentional quasi-geostrophic models introduced by Busse, the velocity and temperature are approximated by

$$\boldsymbol{u} = -\nabla \times V(x, y)\,\boldsymbol{e}_z + \boldsymbol{u}'(\boldsymbol{r}), \hat{T} = \hat{T}(x, y), |\boldsymbol{u}'| \ll |\nabla \times V\,\boldsymbol{e}_z|. \tag{2.5}$$

The angles of inclination, θ_T and θ_B, have absolute magnitudes much less than 1. The basic temperature profile is taken as $\widetilde{T}(y) = y$. Under these assumptions the z-averaged z-vorticity equation becomes

$$\frac{\partial \nabla^2 V}{\partial t} + J(V, \nabla^2 V) - \beta \frac{\partial V}{\partial x} = -\frac{Ra}{Pr} \frac{\partial \hat{T}}{\partial x} - C|\beta|^{1/2}\nabla^2 V + \nabla^2\nabla^2 V, \tag{2.6}$$

where the Rayleigh number $Ra = Pr\,Ra'/E = \alpha g \Delta T d^3/\nu\kappa$, and the Jacobian is defined by

$$J(A, B) = \frac{\partial A}{\partial x}\frac{\partial B}{\partial y} - \frac{\partial A}{\partial y}\frac{\partial B}{\partial x}. \tag{2.7}$$

The β parameter and the Ekman-layer strength are

$$\beta = 2(\theta_T - \theta_B)\frac{d}{L_z}E^{-1}, \quad C = \left(\frac{2}{|\theta_T - \theta_B|} \frac{d}{L_z} \right)^{1/2}. \tag{2.8}$$

We assume that $\beta > 0$, corresponding to a region outside the tangent cylinder in spherical geometry. We note that specification of (β, C) determines the two numbers

$$\frac{1}{E}\left(\frac{d}{L_z}\right)^2 = \frac{\beta C^2}{4}, \quad \frac{1}{\theta_T - \theta_B}\frac{d}{L_z} = \frac{C^2}{2}. \tag{2.9}$$

However, the geometry is too loosely defined to determine $(E, d/L_z, \theta_T, \theta_B)$. In Rotvig (2006), who considers the effects of curved top and bottom boundaries with finite angle of inclination, this degeneracy is removed. Under the above assumptions the

heat equation (2.1*b*) becomes

$$\frac{\partial \hat{T}}{\partial t} + J(V, \hat{T}) = -\frac{\partial V}{\partial x} + \frac{1}{Pr}\nabla^2 \hat{T}. \tag{2.10}$$

Similarly to spherical geometry, we define the zonal flow by

$$\boldsymbol{u}_Z = \langle u_x \rangle_x \boldsymbol{e}_x = -\frac{\partial \langle V \rangle_x}{\partial y}\boldsymbol{e}_x, \tag{2.11}$$

where again the *z*-dependent component $\boldsymbol{u}'$ has been neglected. The *x*-average is defined by $\langle A \rangle_x = (1/L_x)\int_0^{L_x} A\,\mathrm{d}x$. Key quantities analysed in this paper are the total kinetic energy and the zonal kinetic energy defined by

$$E_k = \frac{1}{L_x}\int (\nabla V)^2\,\mathrm{d}S, \quad E_k^Z = \frac{1}{L_x}\int (\langle \nabla V \rangle_x)^2\,\mathrm{d}S. \tag{2.12}$$

From the kinetic energy we may estimate the Reynolds number by $Re = \sqrt{E_k}$.

For the numerical integration of equations (2.6) and (2.10) we expand the stream-function and temperature in the form

$$A = \sum_{l=-(N_x-1)}^{N_x-1} \sum_{m=1}^{N_y-1} A_{lm}\exp(\mathrm{i}lx(2\pi/L_x))\sin m\pi y. \tag{2.13}$$

This expansion allow us to define an $(\hat{m}+1)$-jet solution as one in which the kinetic energy associated with the $(l, m) = (0, \hat{m})$ mode dominates over all other $(0, m)$ modes most of the time.

In this paper, we investigate solutions to equations (2.6) and (2.10) with $Pr = 1$ and $L_x = 2\pi$. In the following section we undertake an extensive parameter study of the zonal flow. In these simulations $(Ra/Ra_c, \beta, C) \in [1, 10] \times [7.07 \times 10^4, 7.07 \times 10^5] \times [3.16 \times 10^{-3}, 3.16]$. Subsequently, we analyse three specific solutions in greater detail: run Ia denotes a typical two-jet solution at moderate Rayleigh number without boundary friction, $(Ra/Ra_c, \beta, C) = (2.75, 5 \times 10^5, 0)$. Run Ib also has no boundary friction and has parameter values $(Ra/Ra_c, \beta, C) = (2.5, 5 \times 10^5, 0)$ close to run Ia, but the zonal flow is dominated by $m = 2$, i.e. it is a three-jet solution. A multi-jet solution, defined by the zonal flow having a dominating wavenumber $m \geqslant 2$, is uncommon without boundary friction. Run II is a typical multi-jet solution, in this case a six-jet solution, at moderate Rayleigh number including boundary friction, $(Ra/Ra_c, \beta, C) = (2.5, 7.07 \times 10^5, 0.316)$. To ease comparison, this C value is identical to the one used in JRA. All the β-scalings calculated in this paper have $(Ra/Ra_c, C) = (2.5, 0.316)$.

3. Windows of multiple-jet solutions

The annulus model may be viewed as one of the simplest possible models of rapidly rotating convection outside the tangent cylinder in a spherical shell. This simplicity implies efficient computer implementation, and it allows investigation in regimes outside the reach of three-dimensional models. However, there are clearly discrepancies between the present model and the fully three-dimensional case. The form of C is given by equation (2.8), but in more complex models, involving curved boundaries, compressibility and magnetic fields, the functional form of C may alter. Rotvig (2006) analyses a duct with curved top and bottom boundaries. In a simplified version of this system, $\beta(y)$ and $C(y)$ may be identified as the coefficients in front

of $-\partial_x V$ and $-|\beta|^{1/2}\nabla^2 V$, respectively in equation (2.6). Typically, it turns out that $C \in [0.5, 1.5]$. A prerequisite for this system to be able to produce multi-jet solutions is that the present model has this capability with $C \in [0.5, 1.5]$. It is therefore important to know in what ways the results depend on C.

For given β, an extensive parameter study in C requires evaluation of convection onset at many values of (C, l). Doing this by timestepping is impractical. Instead, we may formulate the linear problem as a generalized eigenvalue problem

$$\boldsymbol{A}\boldsymbol{x} = \lambda\boldsymbol{B}\boldsymbol{x}, \tag{3.1}$$

where the time-dependence of the solution is in the form $\boldsymbol{x} \propto \mathrm{e}^{\lambda t}$. At onset of convection $\lambda = -\mathrm{i}\omega$. Two different spectral methods have been employed, (i) Sine expansion in y, equation (2.13), and (ii) Chebyshev expansion in y

$$A = \sum_{l=-(N_x-1)}^{N_x-1} \sum_{m=0}^{N_y+N_A-1} A_{lm}\exp(\mathrm{i}lx(2\pi/L_x))T_m(2y-1), \tag{3.2}$$

where N_A depends on the number of boundary conditions for A. The former method has the advantage of implicit boundary conditions, whereas these conditions must be explicitly specified in the Chebyshev method. In this latter method, the boundary conditions produce rows of zeros in the matrix $\boldsymbol{B}$ which then becomes singular. A Lapack routine has been used to solve equation (3.1) for both methods which compare successfully. The large number of linear problems as a function of (C, l) allows efficient parallelization in the (C, l)-plane. The result for $\beta = 3.16 \times 10^5$ is shown in figure 2 where we have explored the range from zero boundary friction up to large Ekman-layer strengths. We denote Ra_c of the most unstable l-mode by $Ra_c(C)$. As expected, $Ra_c(C)$ increases for increasing Ekman-layer strength. However, $Ra_c(C)$ has a maximum at $C = 5.2$. This is probably due to an increased x-length-scale of the flow. Figure 2(b) shows the frequency $\omega_c(C, l)$. For $l \leqslant 44$, the lines start to lose their quasi-linear appearance when C is sufficiently small. In the panel, however, only the quasi-linear part of the lines is shown. The frequency of the most unstable l-mode is denoted by $\omega_c(C)$. Near the maximum of $Ra_c(C)$, we observe that $\{C, \omega_c(C)\}$ is close to the region where the ω_c-lines lose their quasi-linear appearance. Finally, we may note that the positive (prograde) phase velocity is slightly slowed down towards higher C. In addition, the group velocity near onset of convection changes sign near the maximum of $Ra_c(C)$ being negative for small Ekman-layer strength.

Based on the knowledge of $Ra_c(C)$, we have performed a nonlinear parameter study in C focusing on the zonal wind and multi-jet aspect of the solutions. The result is shown in table 1. As a starting point, we put $C = 0.316$, as in JRA, and then step C up and down by factors of about 2. Only values of C that produce zonal flows with energy larger than 5 % of the total energy are considered. The lower cutoff in C is at the point where either $C < 3.16 \times 10^{-3}$ or when two successive C-values both result in two-jet solutions. The Ekman dissipation term introduces a second relaxation time $\tau = 1/C|\beta|^{1/2}$. For the simulations in table 1 we have $\tau \in [3.8 \times 10^{-4}, 8.4 \times 10^{-1}]$. This additional relaxation time hence does not imply longer integration times. However, in some cases, e.g. when $(Ra/Ra_c, \beta, C) = (5, 3.16 \times 10^5, 7.07 \times 10^{-3})$ so that $\tau = 0.25$, we observe oscillations in the zonal flow with periods close to τ, but different from the bursting period.

In general, with a few exceptions, we find that decreasing C enhances the zonal flow strength. This result agrees well with the three-dimensional results in Gilman (1978b) and Christensen (2001), where stress-free boundary conditions produce stronger zonal
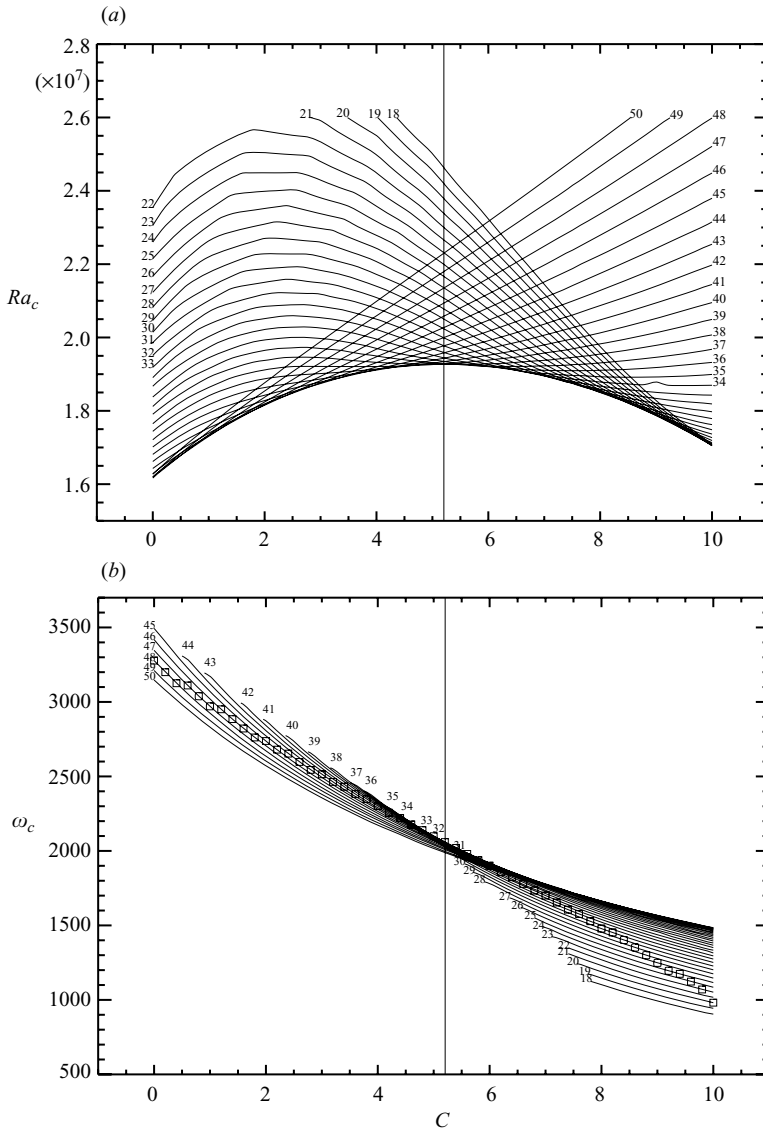
FIGURE 2. The linear problem for $\beta = 3.16 \times 10^5$. (*a*) Critical Rayleigh number Ra_c for onset of convection as a function of the Ekman-layer strength C and the azimuthal mode number l. The latter labels the lines in the panel. (*b*) Frequency of the solutions. The squares give the l-index of the most unstable mode as a function of C. The vertical lines depict the maximum of $Ra_c(C)$, see also text.

flows than non-slip boundaries. Decreasing C, however, also reduces the number of jets. Typically, local depressions in zonal flow strength are located at C-values where a change in the number of jets takes place. This observation was also made in JRA, but as a function of β. At such a location, it may take a long time before the solution has converged. We observe several long C-strides of three-jet solutions. At $(Ra/Ra_c, \beta) = (2.5, 7.07 \times 10^5)$, the first long C-stride of four-jet solutions has emerged.

Subtable: $Ra/Ra_c = 2.5$

C	β			
	7.07×10^4	1.41×10^5	3.16×10^5	7.07×10^5
3.16×10^0				
1.41×10^0				
7.07×10^{-1}	$-$, 2	$-$, 2	$-$, 2	$-$, 3
3.16×10^{-1}	**3** : 15 (65), 14	**3** : 33 (100), 35	**4** : 39 (100), 40	**5** : 44 (100), 48
1.41×10^{-1}	**2** : 53 (100), 55	**3** : 42 (100), 59	**3** : 64 (100), 67	**4** : 62 (100), 63
7.07×10^{-2}	**2** : 74 (100), 75	**2** : 78 (100), 79	**3** : 66 (100), 74	**3** : 77 (100), 80
3.16×10^{-2}	1 : 38 (93), 64	**2** : 81 (100), 82	**2** : 84 (100), 85	**3** : 73 (100), 79
1.41×10^{-2}	1 : 61 (100), 75	**2** : 82 (100), 83	**2** : 87 (100), 89	**3** : 23 (100), 32
7.07×10^{-3}		**2** : 81 (100), 83	**2** : 88 (100), 89	**2** : 60 (100), 79
3.16×10^{-3}		**2** : 81 (100), 83	**2** : 67 (100), 70	**2** : 64 (100), 81

Subtable: $Ra/Ra_c = 5.0$

C	7.07×10^4	1.41×10^5	3.16×10^5	7.07×10^5
3.16×10^0				
1.41×10^0	$-$, 2	$-$, 3	$-$, 3	$-$, 5
7.07×10^{-1}	**2** : 9 (85), 10	**2** : 9 (78), 12	**3** : 27 (100), 30	**4** : 42 (100), 45
3.16×10^{-1}	**2** : 59 (100), 61	**2** : 63 (100), 65	**3** : 66 (100), 67	**4** : 65 (100), 67
1.41×10^{-1}	1 : 81 (100), 84	**2** : 78 (100), 80	**2** : 56 (100), 68	**2** : 54 (92), 70
7.07×10^{-2}	1 : 88 (100), 90	**2** : 81 (100), 82	**2** : 82 (100), 84	**2** : 51 (100), 68
3.16×10^{-2}		1 : 92 (100), 94	1 : 91 (100), 92	**2** : 46 (100), 69
1.41×10^{-2}		1 : 94 (100), 95	**2** : 68 (100), 70	**2** : 67 (100), 68
7.07×10^{-3}			**2** : 69 (100), 70	**2** : 70 (100), 71
3.16×10^{-3}			**2** : 65 (100), 68	1 : 95 (100), 96

Subtable: $Ra/Ra_c = 10.0$

C	7.07×10^4	1.41×10^5	3.16×10^5	7.07×10^5
3.16×10^0			$-$, 2	$-$, 2
1.41×10^0	$-$, 4	$-$, 5	**2** : 6 (53), 11	**4** : 8 (47), 16
7.07×10^{-1}	**2** : 19 (59), 22	**2** : 42 (100), 47	**2** : 39 (100), 42	**3** : 48 (100), 57
3.16×10^{-1}	1 : 29 (78), 36	**2** : 43 (100), 71	**2** : 72 (100), 75	**2** : 59 (100), 66
1.41×10^{-1}	1 : 69 (100), 73	1 : 76 (100), 79	1 : 48 (100), 84	**2** : 72 (100), 76
7.07×10^{-2}		1 : 77 (100), 80	1 : 90 (100), 93	**2** : 75 (100), 77
3.16×10^{-2}				**2** : 75 (100), 78
1.41×10^{-2}				1 : 95 (100), 97
7.07×10^{-3}				1 : 96 (100), 97
3.16×10^{-3}				

TABLE 1. Zonal flow characteristics as a function of $(Ra/Ra_c, \beta, C)$, given as percentages. The three subtables have $Ra/Ra_c = 2.5$, 5.0 and 10.0, respectively. Each entry is defined as follows. The last percentage is the time-averaged ratio of the zonal energy to the total kinetic energy. Where this number is $\leqslant 5\%$ no further information is given (a dash). For a stronger zonal flow, the peak component $m_p(t)$ is studied. The most frequent value m'_p of $m_p(t)$ is given as the first number, which, for clarity, is bold when greater than one. Then follows the time-average (%) of the ratio between the energy of the m'_p component of the zonal flow and the total kinetic energy during its prime time, i.e. when $m_p = m'_p$. Then finally, in parentheses, the ratio between prime time and the total integration time is shown.

Increasing C leads to a rather abrupt cutoff of the zonal flow. For $Ra/Ra_c = 2.5$, this happens at approximately constant C in the β-range investigated. The same is true for $Ra/Ra_c = 5$, but at a higher C and with a steeper increase in the zonal flow strength. For $Ra/Ra_c = 10$, however, the zonal flow cutoff increases with β. In all three cases of the forcing we also note that the cutoff of multi-jet solutions, resulting from decreasing C, decreases with β. Thus windows of C-values, producing strong multi-jet zonal flows, have appeared. These windows widen as β is increased, so they are wedge shaped in the (β, C)-plane. The windows persist to very small values of C. This implies that in more general theories, which may be able to introduce terms similar

to the Ekman-layer term, but these being based on other physical processes, only a weak presence of these processes is required to produce multi-jet solutions. Finally, we may note that the C-windows include realistic values, when these are due to curved boundaries, especially at high forcing and high β. Large values of β, equivalent to small E, are required before these windows appear. This result relates well to Gilman (1978b) and Christensen (2001), who find only two-jet solutions outside the tangent cylinder at relatively high Ekman numbers. Rotvig (2006) demonstrated that in a three-dimensional Boussinesq shell with non-slip boundaries, imposed temperature contrast, and a ratio of 0.35 between the inner and outer radius, multi-jet solutions begin to emerge when $E < 5 \times 10^{-6}$.

4. Zonal force balance and the bursting phenomenon

4.1. *Zonal force balance*

The Reynolds stresses play an important role in the mean flow generation. To find an expression for the Reynolds force we x-average equation (2.6)

$$-\frac{\partial}{\partial y}\left[\frac{\partial \langle u_x \rangle_x}{\partial t}\right] + \langle J(V, \nabla^2 V)\rangle_x = -\frac{\partial}{\partial y}\left[-C|\beta|^{1/2}\langle u_x \rangle_x + \frac{\partial^2 \langle u_x \rangle_x}{\partial y^2}\right], \quad (4.1)$$

where we used (2.5). The nonlinear term is

$$\langle J(V, \nabla^2 V)\rangle_x = \langle e_z \cdot \nabla \times (u \cdot \nabla u)\rangle_x = -\frac{\partial}{\partial y}\langle e_x \cdot (u \cdot \nabla u)\rangle_x = -\frac{\partial}{\partial y}\left\langle \frac{\partial}{\partial x_j}(u_x u_j)\right\rangle_x$$

$$= -\frac{\partial^2}{\partial y^2}\langle u_x u_y \rangle_x. \quad (4.2)$$

Integrating equation (4.1) along y, we obtain the x-averaged x-component of the momentum equation

$$\frac{\partial \langle u_x \rangle_x}{\partial t} = -\frac{\partial}{\partial y}\langle u_x u_y \rangle_x - C|\beta|^{1/2}\langle u_x \rangle_x + \frac{\partial^2 \langle u_x \rangle_x}{\partial y^2}. \quad (4.3)$$

The constant of integration is zero since the zonal mass flux, $\langle u_x \rangle_{xy}$, is zero, see equation (2.13). In equation (4.3) the right-hand-side terms are the Reynolds force, the Ekman-layer drag, and the bulk viscous force, respectively.

4.2. *Energy fluctuations*

Energy rates of change provide estimates of various force balances. In order to obtain an expression for the time-derivative of the kinetic energy (2.12), we first rewrite it as

$$E_k = \frac{1}{L_x}\int (\nabla V)^2 \, dS = -\frac{1}{L_x}\int V\nabla^2 V \, dS. \quad (4.4)$$

We can show that

$$\int \frac{\partial V}{\partial t}\nabla^2 V \, dS = \int V\frac{\partial \nabla^2 V}{\partial t} \, dS. \quad (4.5)$$

So

$$\frac{dE_k}{dt} = -\frac{2}{L_x}\int V\frac{\partial \nabla^2 V}{\partial t} \, dS. \quad (4.6)$$

We split the energy rate of change into the following components

$$\frac{dE_k}{dt} = \frac{dE_k^B}{dt} + \frac{dE_k^E}{dt} + \frac{dE_k^V}{dt}, \quad (4.7)$$

where the time-derivatives,

$$\dot{E}_k^B = \frac{2Ra}{L_x Pr} \int V \frac{\partial \hat{T}}{\partial x}\, \mathrm{d}S, \quad \dot{E}_k^E = -\frac{2C|\beta|^{1/2}}{L_x} \int (\nabla V)^2\, \mathrm{d}S, \quad \dot{E}_k^V = -\frac{2}{L_x} \int (\nabla^2 V)^2\, \mathrm{d}S, \tag{4.8}$$

are the power input from the buoyancy force, the viscous dissipation by the Ekman drag, and the dissipation by the bulk viscous force, respectively.

4.3. *Symmetry*

We note that a solution $(V, \hat{T})$ to equations (2.6) and (2.10) that satisfies the boundary conditions provides us with a solution $(V_2, \hat{T}_2)$ to the same problem but with β replaced by $-\beta$

$$(V_2, \hat{T}_2)|_{(x,y)} = (-V, \hat{T})|_{(L_x - x, y)}. \tag{4.9}$$

This solution is a reflection of the original one about $x = L_x/2$ and with a sign change in the velocity potential. The velocity becomes $(u_{2x}, u_{2y})|_{(x,y)} = (-u_x, u_y)|_{(L_x - x, y)}$.

In contrast to the fully three-dimentional problem, the annulus has a symmetry along the radial direction. For a solution $(V, \hat{T})$ to equations (2.6) and (2.10) satisfying the boundary conditions, there exists a second solution $(V_3, \hat{T}_3)$ to the same system

$$(V_3, \hat{T}_3)|_{(x,y)} = -(V, \hat{T})|_{(x, 1-y)}, \tag{4.10}$$

obtained by reflection about $y = 1/2$ and with sign changes in both the velocity potential and temperature. The velocity of the new solution is $(u_{3x}, u_{3y})|_{(x,y)} = (u_x, -u_y)|_{(x, 1-y)}$. This means that for a zonal flow with m odd, so that the zonal flow changes sign about $y = 1/2$, the annulus model cannot determine the overall sign of the zonal flow. As noted by Busse (2002), this symmetry is destroyed in the curved annulus model (Busse & Hood 1982), which in its simplest form replaces β by $\beta_0 + (y - 1/2)\beta_1$. They show that the spherical case, $\beta_1 < 0$, leads to positive (prograde) flow at $y = 0$ and negative flow at $y = 1$, in agreement with fully three-dimensional spherical shell simulations (Christensen 2002).

4.4. *The bursting phenomenon*

In run Ia, in which the zonal flow is positive at $y = 0$, periodically enhanced Reynolds forces, induced by bursts of convective flow, reinforce the zonal flow (see figures 3, 4*a, b*). In the intermediate quiet periods, the zonal flow $\langle u_x \rangle_x$ provides a strong shear, suppressing the convective flow u_y. The Reynolds force is not strong enough to overcome viscous dissipation and the zonal flow decays exponentially. Eventually, the weakened shear permits a new discharge of convection, thereby increasing the Reynolds force and the zonal flow. The recovered shear turns off convection and the cycle repeats. This type of phenomenon is hence a relaxation oscillation.

These intermittent discharges of convection occur in several different geometries. In the present geometry, it was first noted by Brummell & Hart (1993). Grote & Busse (2001), and Christensen (2001, 2002) observed it in a spherical shell at intermediate Rayleigh numbers. As seen in figure 4(*b*), a burst is asymmetric in the radial y-direction being strongest in the inner half of the container. At maximum, the convective flow nearly fills the entire volume, except for weak regions near the walls.

A burst precursor may be seen in the (t, y)-dependent r.m.s. of the temperature $\sqrt{\langle \hat{T}^2 \rangle_x}$ (see figure 4*e*). This quantity builds up linearly in time at the outer wall. At burst onset, the precursor of enhanced temperature fills a quarter of the container. During the burst, the temperature is highest in the inner half of the container. After
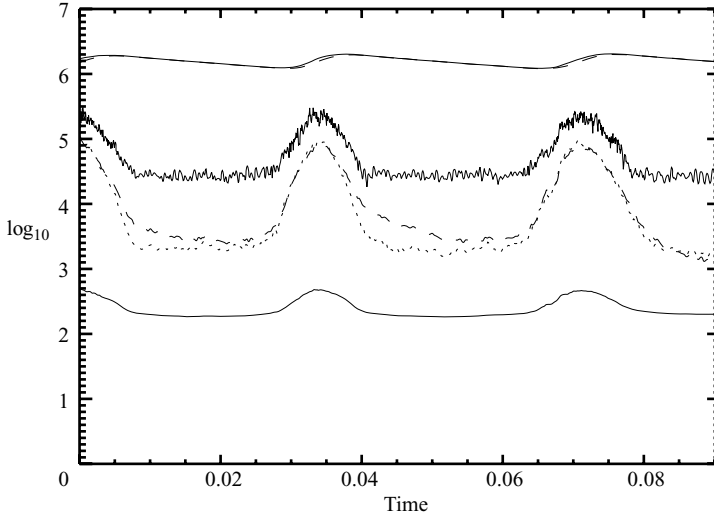
FIGURE 3. Run Ia. From above we have total kinetic energy E_k (solid), zonal kinetic energy E_k^Z (dashed) which is almost the entire energy, r.m.s. mean Reynolds force $\sqrt{\langle|\partial_y\langle u_x u_y\rangle_x|^2\rangle_y}$ (solid), kinetic energy of $u_x - \langle u_x\rangle_x$ (dashed), kinetic energy of u_y (dotted), and r.m.s. temperature $\sqrt{\langle\hat{T}^2\rangle_{xy}}$ (solid). These quantities are plotted on a logarithmic scale. For clarity, the r.m.s. temperature has been displaced by 4.0 on the logarithmic scale.

the convective discharge, the enhanced temperature decays rapidly in the outer half, whereas a strong long-lasting afterglow is observed in the inner half of the container. The precursor may be related to the x-dependence of the thermal boundary layers being much stronger at the outer than at the inner wall (see figure 4c). Figure 4(d) shows the long radial plumes during a burst. The afterglow may help to suppress convection, and so bursts do not appear until both the shear and the afterglow have diffused away. The z-component of the vorticity is $w = (\nabla \times \boldsymbol{u})_z = \nabla^2 V$. In figure 4($f$) we observe that the generation of mean vorticity $\langle w\rangle_x$ is strongest near the walls. However, these vortices rapidly leave the walls, maintaining a mean vorticity in the interior.

Without boundary friction, multi-jet solutions are rare for $\beta < 10^6$. In a narrow window of the Rayleigh number, $Ra/Ra_c \in [2.00, 2.75]$ at $\beta = 5.0 \times 10^5$, two-jet solutions are produced at the end points, whereas a three-jet zonal flow is found at $Ra/Ra_c = 2.5$ (see figure 5a and JRA). The zonal component contains 88 % of the total kinetic energy. As in run Ia, the burst phenomenon is strong.

In run Ib we also observe a large-scale $m = 3$ wave in u_x, with wavelength around 6.2 in the x-direction, which persists for longer ducts, $L_x = 4\pi, 8\pi$. The $m = 3$ nature of this wave can be seen in figure 5(a): the negative zonal flow is enhanced (reduced) at $y = 1$ ($y = 0$) for $x \in [1, 3]$. Here, the positive central jet is at maximum upward displacement. If the wave were dominated by an $m = 1$ mode, the central jet would have been displaced downwards in this region. Figure 5(b) shows the energy density of u_x along $x = 3.13$ and figure 5(c) the same quantity along $y = 0.65$. From figure 5(c) we determine the angular frequency $\omega \sim 2\pi/0.0012 = 5.2 \times 10^3$ and the wavenumber $k \sim 2\pi/6.2 = 1.0$. Rossby and thermal Rossby waves fit these (ω, k) values reasonably well. A discussion of Rossby waves in the β-plane model may be found in, for example, Stewartson (1978). Assuming a small perturbation of the linear part of inertia and
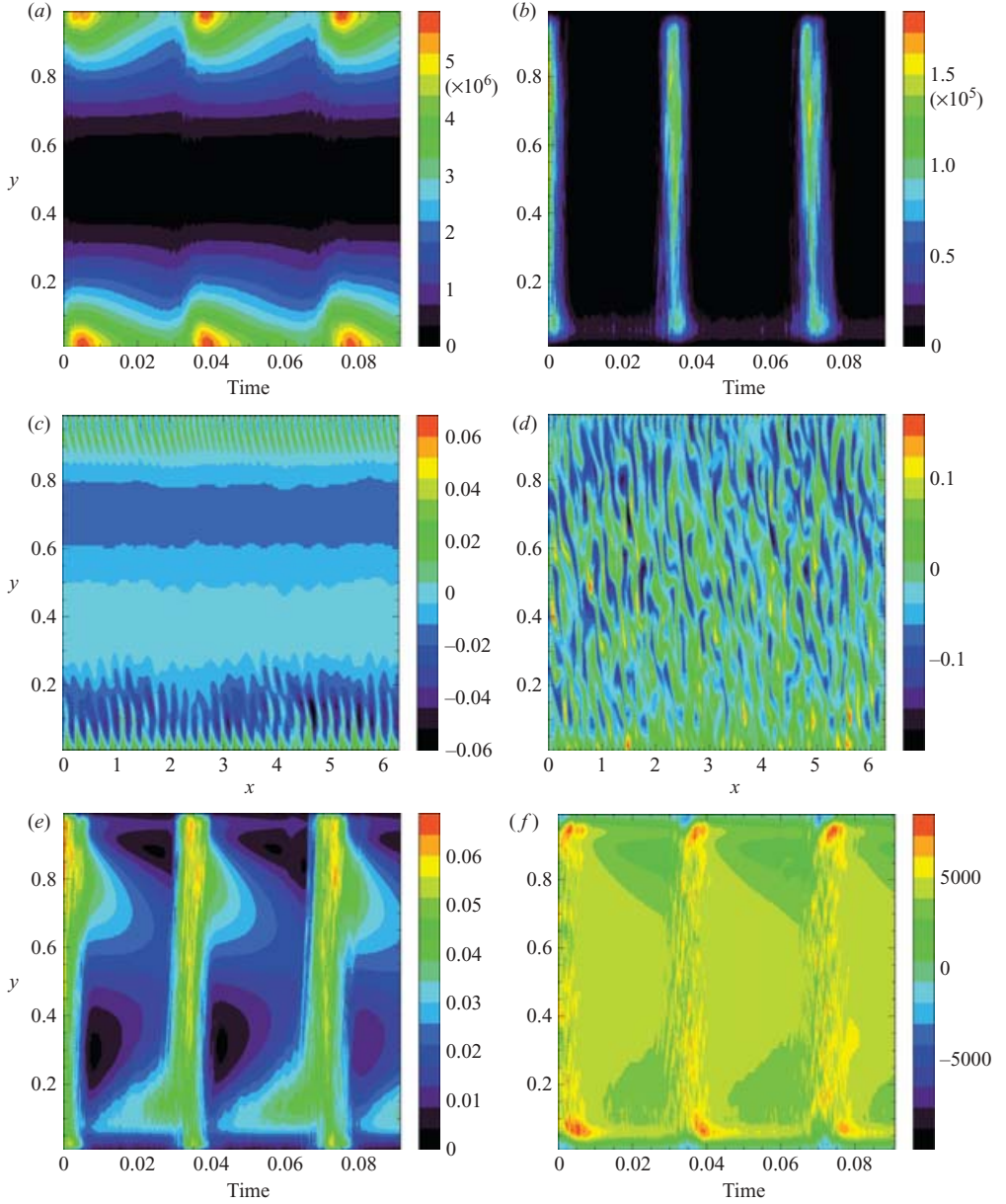
J. Rotvig and C. A. Jones

FIGURE 4. Run Ia. (*a*) Mean kinetic energy density $\langle u_x^2 \rangle_x (t, y)$. (*b*) Mean kinetic energy density $\langle u_y^2 \rangle_x (t, y)$. (*c*) Temperature $\hat{T}(x, y)$ for a quiet state. (*d*) Temperature $\hat{T}(x, y)$ a burst. (*e*) Root mean square temperature $\sqrt{\langle \hat{T}^2 \rangle_x}$ as function of (t, y). (*f*) Mean vorticity $\langle w \rangle_x$ in the (t, y)-plane.

the Coriolis force in the form

$$A = A_0 \exp(\mathrm{i}(kx - \omega t)) \sin m\pi y, \tag{4.11}$$

we obtain Rossby waves with dispersion relation

$$\omega = \frac{\beta k}{k^2 + m^2 \pi^2}. \tag{4.12}$$
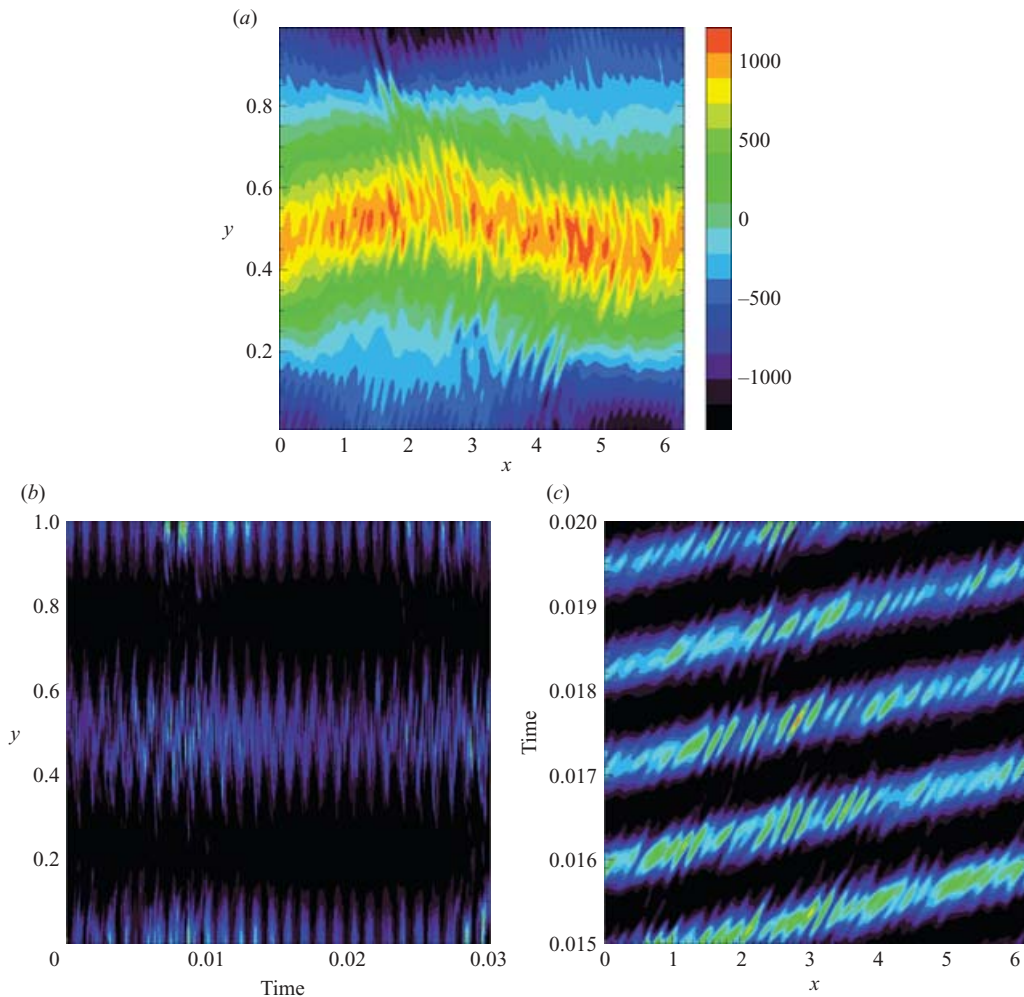
FIGURE 5. Run Ib. Multi-jet solution with zero boundary friction. (*a*) The velocity component $u_x(x, y)$. (*b*) Kinetic energy density u_x^2 along $x = 3.13$ in the (t, y)-plane. (*c*) Kinetic energy density u_x^2 along $y = 0.65$ in the (x, t)-plane.

Busse (1994) derives the solution at onset of convection. Therein the streamfunction and temperature are in the form (4.11) by ansatz. The critical value of (Ra, ω, k) as a function of β is then determined. Here we consider a small perturbation in the form of a thermal Rossby wave, but for given $(\beta, Ra, k) = (5 \times 10^5, 7.8 \times 10^7, 1.0)$. In the neighbourhood of this point, the dispersion relation of the thermal Rossby wave takes the form (4.12) to a good approximation. In our case with $m = 3$, the frequency becomes $\omega \sim 5.6 \times 10^3$, which is not far from the observed value. Since the period of the wave is of the same order of magnitude as the duration of a burst, it may be that this wave is generated by the convective bursts.

In run II, the burst phenomenon is absent (see figure 6*a*). Plots of the quantities in figure 3 for run II also appear quasi-stationary. Figure 6(*b*) illustrates the suppression of convection in regions with strong shear. In other cases, the boundary friction typically damps the convective bursts as well, but not always as fully as in run II.
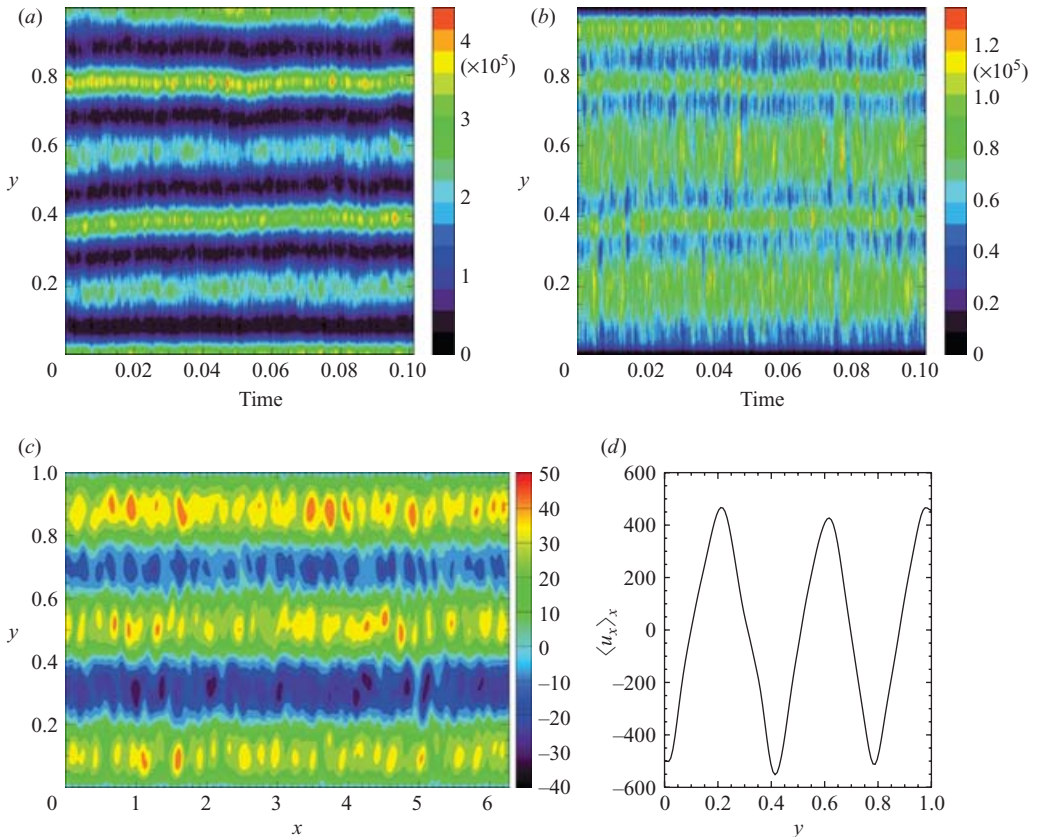
FIGURE 6. Run II. (*a*) Mean kinetic energy density $\langle u_x^2 \rangle_x (t, y)$. (*b*) Mean kinetic energy density $\langle u_y^2 \rangle_x (t, y)$. (*c, d*) Snapshots of the solution: (*c*) velocity potential $V(x, y)$, and (*d*) zonal flow $\langle u_x \rangle_x$.

For the runs in table 1, we typically find bursting solutions when the Ekman-layer strength is an order of magnitude smaller than the upper cutoff of the zonal flow.

4.5. *Balances of energy fluctuations, and balances of zonal forces*

In run Ia, the energy decays in intervals between bursts owing to the small buoyancy energy input (see figure 7). During bursts, the leading balance in the energy fluctuations is between buoyancy and bulk viscosity, giving a small overall positive energy rate of change. The situation in run II is somewhat similar, see the dashed curve in figure 8(*a*). The main balance is between the buoyancy energy input and bulk dissipation (as during a burst in run Ia), and the total energy rate of change is now negligible, as expected in a quasi-steady state. The energy dissipation caused by the viscous boundary layers is an order of magnitude smaller than the leading terms.

At $(Ra/Ra_c, C) = (2.5, 0.316)$, the computational costs involved in searching for β-scalings are manageable. We have considered the interval $\beta \in [7.07 \times 10^3, 7.07 \times 10^6]$, which also includes run II. As seen in figure 8(*a*), the Ekman dissipation remains of second order up to large β. However, as shown in table 1, the effect of the zonal Ekman dissipation is still quite dramatic: (i) The zonal flow strength is weakened, and (ii) Multi-jet solutions are much more easily produced at high β. Figure 8(*b*) shows that Ekman dissipation becomes dominant over bulk dissipation as the forcing
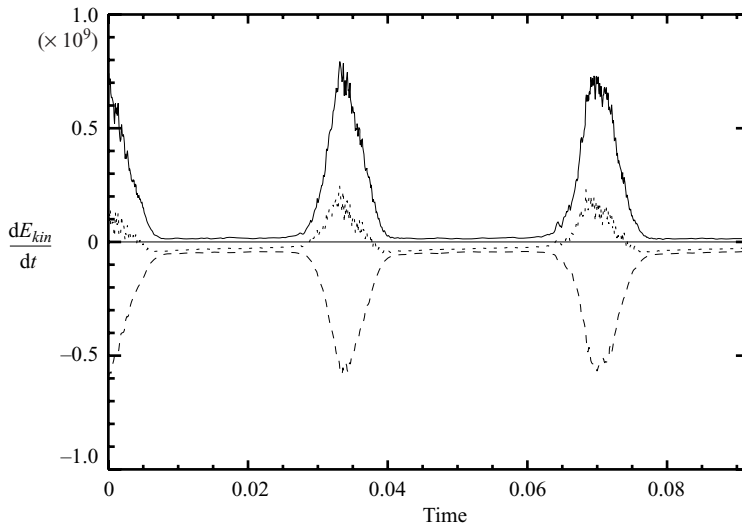
FIGURE 7. Run Ia. Energy rate of changes as function of time. The quantities are dE_k/dt
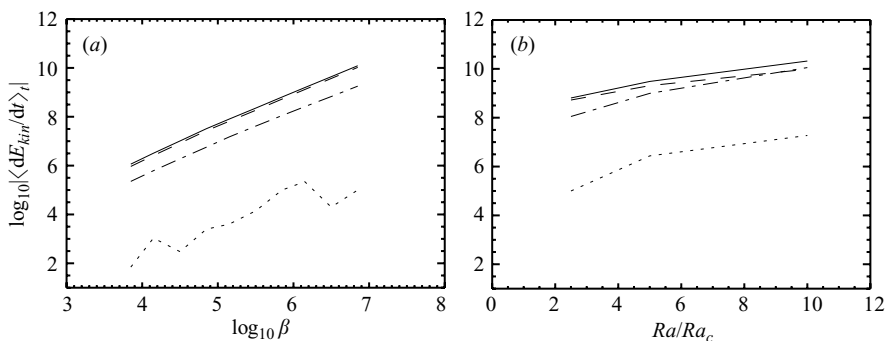(dotted), dE_k^B/dt (solid), and dE_k^V/dt (dashed).

FIGURE 8. Time-averaged energy rate of changes as function of (a) β at $Ra/Ra_c = 2.5$, and
(b) Ra/Ra_c at $\beta = 7.07 \times 10^5$. The quantities are dE_k/dt (dotted line), dE_k^B/dt (solid line),
dE_k^V/dt (dashed line), and dE_k^E/dt (dash-dotted line). The Ekman-layer strength $C = 0.316$.

strength is increased for fixed β. The increased forcing implies an increased strength
of the zonal flow, but the ability of the Ekman layers to create multi-jets has
diminished (see table 1). Figure 9 shows the β-dependence of various quantities. For
$\beta \in [1.41 \times 10^6, 7.07 \times 10^6]$ these scale as

$$\left.\begin{array}{l} E_k = 18\beta^{0.70}, \ E_k^Z = 3.1\beta^{0.77}, \ E_{kin}(u_x - \langle u_x \rangle_x) = 14\beta^{0.61}, \ E_{kin}(u_y) = 15\beta^{0.62}, \\[2mm] \sqrt{\langle \hat{T}^2 \rangle_{xy}} = 4.1\beta^{-0.35}, \ \sqrt{\langle |\partial_y \langle u_x u_y \rangle_x|^2 \rangle_y} = 0.84\beta^{0.93}, \ m_p' = 0.068\beta^{0.32}. \end{array}\right\} \quad (4.13)$$

In this β-interval, the zonal energy is still growing relative to the total energy, whilst
the energy $E_{kin}(u_x - \langle u_x \rangle_x)$ and the convective energy are declining. Based on equation
(4.13), we may compare the Ekman-layer dissipation to the Reynolds force in the
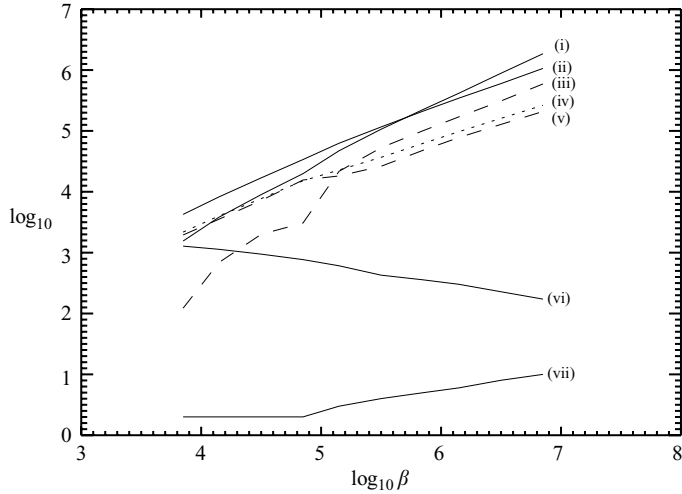
FIGURE 9. β-sequence at $(Ra/Ra_c, C) = (2.5, 0.316)$. The depicted quantities are those in figure 3 and also the dominating mode index of the zonal flow m'_p. The r.m.s. temperature has been displaced by 4.0 on the logarithmic scale. (i) $\sqrt{\langle |\partial_y \langle u_x u_y \rangle_x|^2 \rangle_y}$; (ii) E_k; (iii) E_k^Z; (iv) $E_{kin}(u_y)$; (v) $E_{kin}(u_x - \langle u_x \rangle_x)$; (vi) $\sqrt{\langle \hat{T}^2 \rangle_{xy}}$; (vii) m'_p

zonal flow equation (4.3)

$$\frac{C\beta^{1/2}|\langle u_x \rangle_x|}{|\partial_y \langle u_x u_y \rangle_x|} = 0.66\beta^{-0.045}, \tag{4.14}$$

which is 0.32 at $\beta = 7.07 \times 10^6$. As seen in figure 6(*d*), the first-order derivative of the zonal flow $\partial_y \langle u_x \rangle_x$ is almost a step function and $|\partial_y \langle u_x \rangle_x|$ is quasi-constant. This makes it difficult to estimate the second-order derivative. From equation (4.13), we find that the length-scale of the zonal flow scales as $\beta^{-0.32}$. A crude estimate of the Ekman-layer dissipation to the bulk viscous dissipation is hence $C\beta^{1/2}|\langle u_x \rangle_x|/|\partial_{yy}\langle u_x \rangle_x| \sim \beta^{1/2 - 2 \times 0.32} = \beta^{-0.14}$. Taken together, the above estimates may suggest a balance between the mean Reynolds force and the mean Ekman-layer dissipation. However, these terms will eventually be balanced by an increasing mean bulk dissipation at larger β. In this situation, the length scale of the zonal flow will change, $m'_p \sim \beta^{1/4}$, maintaining the new balance between the zonal forces (see Morin & Dormy 2006).

5. Taylor's condition and geostrophic velocity

Originally, Taylor's condition was associated with the magnetic field in electrically conducting and inviscid flows (Taylor 1963). In the present paper, however, where Reynolds stresses play an important role, it is also of interest to look at Taylorization of the nonlinear part of inertia. A. M. Soward (personal communication 2001) has given an elegant proof of Taylor's condition in the non-plane-parallel case. The modification of this proof for the plane-parallel case is described in Appendix A of Rotvig & Jones (2002). In the present geometry, the adjustment of the original proof is straightforward because here, the top and bottom boundaries are nearly, but not exactly, plane-parallel. Below, we describe the necessity of Taylor's condition. The sufficiency is described in Soward (2001).
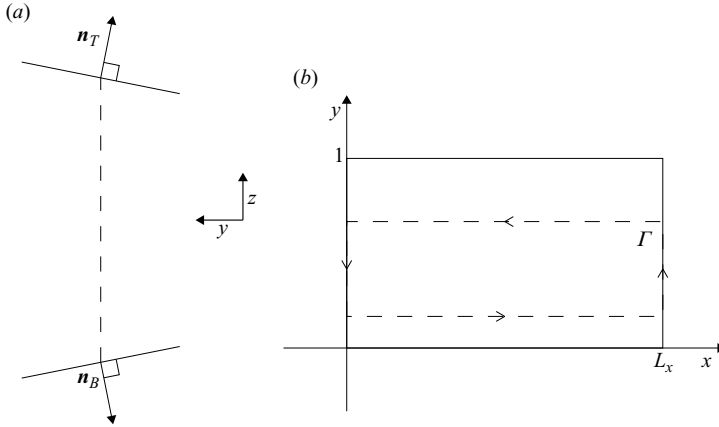
FIGURE 10. Taylor's condition. (*a*) A Taylor (x, z)-plane (dashed) along a geostrophic contour. The vectors $\boldsymbol{n}_T$, $\boldsymbol{n}_B$ are orthogonal to the top and bottom surface, respectively. (*b*) A closed integration path Γ used in Taylor's condition.

Equation (2.1*a*), with the linear part of inertia and the viscous force being neglected, may be written as

$$\boldsymbol{e}_z \times \boldsymbol{u} = -\nabla P + \boldsymbol{G}, \qquad (5.1a)$$

$$\boldsymbol{G} = -\frac{E}{2}\left\{(\nabla \times \boldsymbol{u}) \times \boldsymbol{u} + \frac{Ra}{Pr}T\boldsymbol{e}_y\right\}. \qquad (5.1b)$$

We have merged the gradient component of $\boldsymbol{u} \cdot \nabla \boldsymbol{u}$ with the pressure force and then rescaled P by a factor 2. Only when $\boldsymbol{G}$ satisfies Taylor's condition is it possible to find solutions $(\boldsymbol{u}, P)$ to equation (5.1*a*) that satisfy no-penetration boundary conditions. We parameterize the top and bottom boundary by $f : (x, y) \rightarrow \{x, y, f(x, y)\}$ and $g : (x, y) \rightarrow \{x, y, g(x, y)\}$, respectively. Thus, perpendicular outward directed vectors are $\boldsymbol{n}_T = -\nabla f + \boldsymbol{e}_z$ and $\boldsymbol{n}_B = \nabla g - \boldsymbol{e}_z$ (see figure 10*a*). No-penetration boundary conditions are, $\boldsymbol{n}_T \cdot \boldsymbol{u}_T = 0$, $\boldsymbol{n}_B \cdot \boldsymbol{u}_B = 0$. The specific integral along the z-axis is $\langle A \rangle = \int_g^f A \, \mathrm{d}z'$. Taking this integral of equation (5.1*a*) we find

$$\boldsymbol{e}_z \times \langle \boldsymbol{u} \rangle = -\{\nabla\langle P \rangle + \boldsymbol{n}_T P_T + \boldsymbol{n}_B P_B\} + \langle \boldsymbol{G} \rangle. \qquad (5.2)$$

The quantity $\boldsymbol{H} = \langle \boldsymbol{G} \rangle - \boldsymbol{n}_T P_T - \boldsymbol{n}_B P_B$ satisfies $\nabla \times \boldsymbol{H} = 0$. Thus, any closed path integral of $\boldsymbol{H}$ is zero. In particular, path integrals along closed geostrophic contours reduce to

$$\oint \langle \boldsymbol{G} \rangle \cdot \mathrm{d}\boldsymbol{l} = 0, \qquad (5.3)$$

since $\mathrm{d}\boldsymbol{l} \parallel \boldsymbol{n}_T \times \boldsymbol{n}_B$, see also below. Equation (5.3) is Taylor's condition. The sufficiency of this condition is more complicated to show. Here, we note only that Soward constructs a single-valued solution

$$\boldsymbol{u} = -\nabla \times \boldsymbol{Q} + \tfrac{1}{2}(\boldsymbol{n}_T \times \nabla\Phi_B - \boldsymbol{n}_B \times \nabla\Phi_T), \qquad (5.4a)$$

$$P = \boldsymbol{e}_z \cdot \boldsymbol{Q} + \tfrac{1}{2}(\Phi_T + \Phi_B), \qquad (5.4b)$$

$$\boldsymbol{Q} = \tfrac{1}{2}\left[\int_g^z \boldsymbol{G} \, \mathrm{d}z' - \int_z^f \boldsymbol{G} \, \mathrm{d}z'\right], \qquad (5.4c)$$

to equation (5.1a) where Φ_T and Φ_B are functions of (x, y). These functions are determined by integrating the no-penetration boundary conditions

$$(\boldsymbol{n}_T \times \boldsymbol{n}_B) \cdot \nabla \Phi_T = -\boldsymbol{n}_T \cdot \nabla \times \langle \boldsymbol{G} \rangle, \tag{5.5a}$$

$$(\boldsymbol{n}_T \times \boldsymbol{n}_B) \cdot \nabla \Phi_B = \boldsymbol{n}_B \cdot \nabla \times \langle \boldsymbol{G} \rangle, \tag{5.5b}$$

along geostrophic contours.

A solution to equation (5.1a) is determined only up to a geostrophic flow, i.e. any solution $(\boldsymbol{u}, P)$ to the homogeneous equation where $\boldsymbol{G} = \boldsymbol{0}$. Greenspan (1968) shows that the geostrophic flow is in the form

$$\boldsymbol{u}_G = -\frac{\mathrm{d}\Phi}{\mathrm{d}h}\boldsymbol{n}_T \times \boldsymbol{n}_B, \tag{5.6}$$

where Φ depends only on the height $h = f - g$. In our model, we may therefore define the geostrophic velocity as

$$\boldsymbol{u}_G = \langle u_x \rangle_{xz}\boldsymbol{e}_x = -\frac{\partial \langle V \rangle_x}{\partial y}\boldsymbol{e}_x, \tag{5.7}$$

where we neglected the z-dependent component $\boldsymbol{u}'$. The geostrophic flow is hence identical to the zonal flow (2.11).

In the duct, the path integral in Taylor's condition (5.3) is taken along constant height contours and segments of $x = 0$ and $x = L_x$ (see figure 10b). The condition then becomes

$$\langle \{(\nabla \times \boldsymbol{u}) \times \boldsymbol{u}\}_x \rangle_x = \text{const.} \tag{5.8}$$

The constant is zero, since

$$A = \{(\nabla \times \boldsymbol{u}) \times \boldsymbol{u}\}_x = -\left(\frac{\partial u_y}{\partial x} - \frac{\partial u_x}{\partial y}\right)u_y = -\nabla^2 V \frac{\partial V}{\partial x} = 0 \ (y = 0, 1). \tag{5.9}$$

For a zonal flow, we note that $A = 0$ uniformly. The usual way of defining the Taylorization as a measure of Taylor integrand cancellation along the rotation axis (see e.g. Fearn 1998) does not work in the present case since here no z-averaging is involved in equation (5.8). Instead, we define the flow Taylorization as

$$Tay = \frac{1}{\beta}\frac{\sqrt{\langle |\langle A \rangle_x|^2 \rangle_y}}{E_k} = \frac{1}{\beta}\frac{\sqrt{\langle |\partial_y \langle u_x u_y \rangle_x|^2 \rangle_y}}{E_k}, \tag{5.10}$$

where the β-dependence of the Ekman number has been retained. Care has been taken to make this form independent of the flow strength. In a system with finite viscosity, the zonal flow component of a Taylor flow would rapidly decay away, see equation (4.3).

In figure 11, the Taylorization for run Ia is shown as a function of time. We note that Tay increases weakly during quiet periods. This is due to a decaying kinetic energy, but constant mean Reynolds force (see figure 3). During bursts, Tay increases temporarily by an order of magnitude. This growth is counteracted by an increasing kinetic energy. However, the convection forms of the burst result in strong mean Reynolds forces, and hence rapidly drives up the Taylorization.

At $(Ra/Ra_c, C) = (2.5, 0.316)$, we may derive the β-scaling of the Taylorization from equation (4.13)

$$Tay \sim \beta^{0.93-1-0.70} = \beta^{-0.77}, \tag{5.11}$$

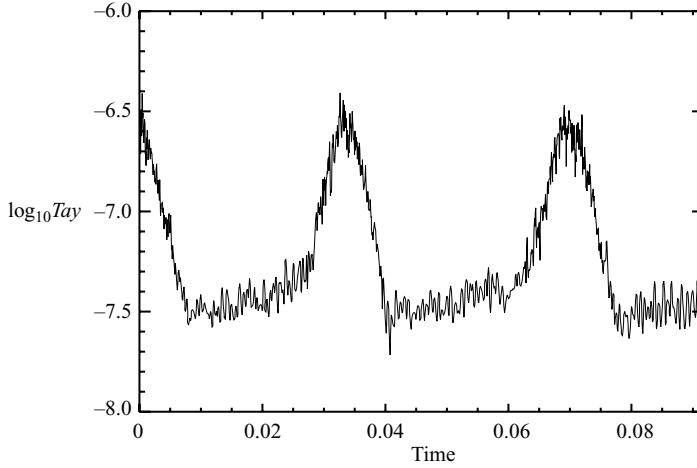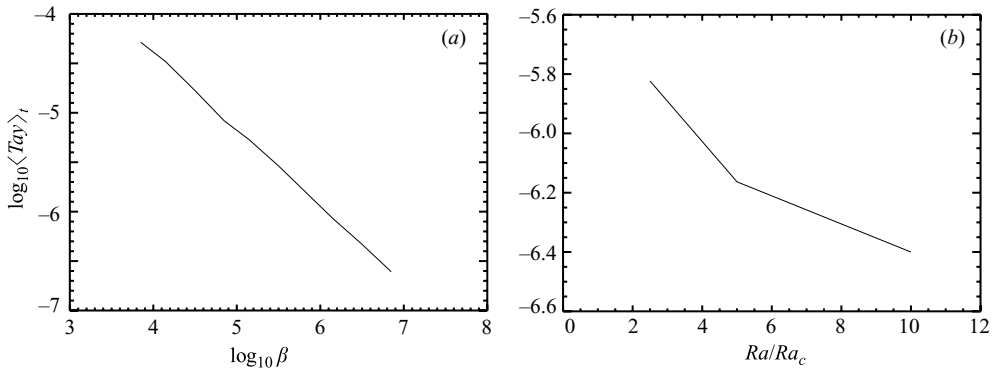FIGURE 11. Run Ia. Taylorization as a function of time.

FIGURE 12. Time-averaged Taylorization as function of (a) β at $Ra/Ra_c = 2.5$, and (b) Ra/Ra_c at $\beta = 7.07 \times 10^5$. The Ekman layer strength $C = 0.316$.

see also figure 12(a). The relatively weak exponent ($\geqslant -1$) confirms that the zonal and non-zonal parts of the flow are comparable in this case. When increasing the forcing at constant β, we expect *Tay* to decrease significantly owing to an increased zonal flow component. This is confirmed by figure 12(b). The three runs at $Ra/Ra_c = 2.5$, 5.0. and 10.0 have kinetic energy $E_k = 2.1 \times 10^5$, 1.9×10^6 and 2.1×10^7, respectively. The r.m.s. mean Reynolds force is increasing less steeply, $\sqrt{\langle|\partial_y\langle u_x u_y\rangle_x|^2\rangle_y} = 2.2 \times 10^5$, 9.1×10^5 and 6.0×10^6, indicating the approach towards a flow Taylor state.

6. Convection length scale

Figure 13 shows the spectrum of the kinetic energy

$$E_k = \sum_{l=-(N_x-1)}^{N_x-1} \sum_{m=1}^{N_y-1} \frac{1}{2} \left(k_x^2 + k_y^2\right) |V_{lm}|^2, \qquad (6.1)$$
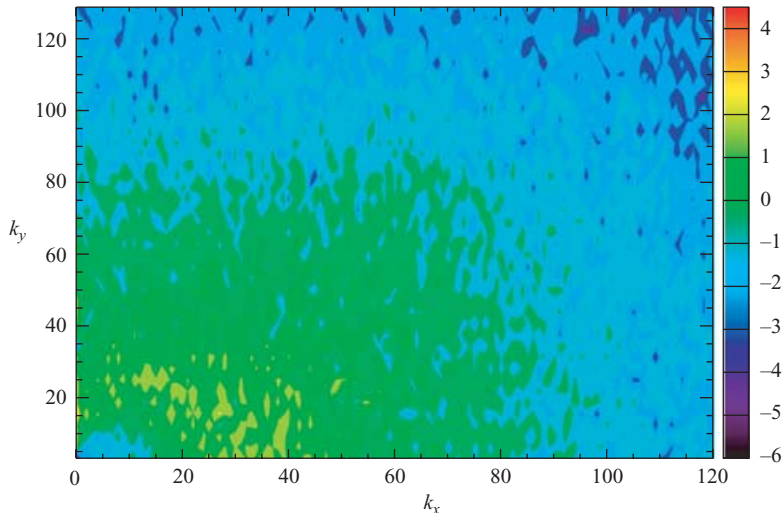
FIGURE 13. Run II. Snapshot of the kinetic energy spectrum $\log_{10}((k_x^2 + k_y^2)|V_{lm}|^2/2)$.

for a snapshot of run II, where the wavenumbers $(k_x, k_y) = (2\pi l/L_x, \pi m)$. We note the peak of the zonal flow at $(k_x, k_y) = (0, 5\pi)$. Aside from this peak, the energy spectrum is roughly symmetric along $k_x = k_y$, implying that typical length scales in the x- and y-direction are comparable. This observation is common in the numerical simulations which usually require an l-resolution three times larger than the m-resolution. We denote this length scale by L. This symmetry is slightly surprising because at onset of convection $(l, m) = (0.67\beta^{0.34}, 1)$, see JRA. This feature may explain the minor asymmetry between the square $(k_x, k_y) \in [20, 40] \times [0, 20]$ and its reflection $(k_x, k_y) \in [0, 20] \times [20, 40]$. Clearly, L is much smaller than the radial length scale associated with the zonal flow. We take the view that L is the dynamical length scale on which convection operates. The convection vortices hence have a quasi-circular shape in the (x, y)-plane. Below, we determine the β-scaling of L.

The following scale analysis is based on balances in the z-vorticity equation (2.6) and the heat equation (2.10) operating in the nonlinear regime. Balancing the z-vorticity advection, the inviscid Coriolis term, and the buoyancy term we have

$$|J(V, \nabla^2 V)| \sim \beta \left|\frac{\partial V}{\partial x}\right|, \beta \left|\frac{\partial V}{\partial x}\right| \sim Ra \left|\frac{\partial \hat{T}}{\partial x}\right|. \tag{6.2}$$

The balance of the Coriolis and buoyancy forces was also found by Aubert *et al.* (2001). A balance between the temperature advection and the basic state term gives

$$|J(V, \hat{T})| \sim \left|\frac{\partial V}{\partial x}\right|. \tag{6.3}$$

Equations (6.2) and (6.3) may be rewritten as

$$\frac{u_x u_y}{L^2} + \frac{u_x^2}{LL_0} \sim \beta u_y, \beta u_y \sim Ra \left|\frac{\partial \hat{T}}{\partial x}\right|, \left|\frac{\partial \hat{T}}{\partial x}\right| \sim \frac{u_y}{u_x}, \tag{6.4}$$

respectively. We made use of $u_x \gg u_y$. This is a good approximation in the $(Ra/Ra_c, C) = (2.5, 0)$ case: in figure 3, where $u_x \sim \langle u_x \rangle_x$, we observe $u_x - \langle u_x \rangle_x \sim u_y$. In

a similar figure for run II, where $u_x \sim 1.7\langle u_x \rangle_x$, we also find $u_x - \langle u_x \rangle_x \sim u_y$, so that the zonal energy is approximately half the total kinetic energy. In equation (6.4), we introduced the radial length scale L_0 ($\geqslant L$) of u_x which may be different from L in the case of a strong zonal flow, $u_x \sim < u_x >_x$. In this latter case, L_0 is known from the number of jets in the zonal flow. Since $Ra \sim \beta^{4/3}$, see JRA, the system (6.4) constitutes three equations in four unknowns ($u_x, u_y, |\partial_x \hat{T}|, L$). We may rearrange equation (6.4)

$$u_x \sim \beta^{1/3}, \; u_y \sim \beta^{-1/3} \frac{L}{\{L^2 + O(\beta^{-2/3})\}L_0}, \; \left|\frac{\partial \hat{T}}{\partial x}\right| \sim \beta^{-2/3} \frac{L}{\{L^2 + O(\beta^{-2/3})\}L_0}. \quad (6.5)$$

Clearly, we must determine L. Equation (6.5) suggests that the convection length scale should not be far away from $L \sim \beta^{-1/3}$. We confirm this by application of the mean Reynolds force scaling

$$|\partial_y \langle u_x u_y \rangle_x| \sim \frac{1}{\{L^2 + O(\beta^{-2/3})\}L_0} \sim \beta^{\lambda_{RF}}, \quad (6.6)$$

where we used $\partial_y(u_x u_y) \sim u_x u_y / L_0 + u_x u_y / L \sim u_x u_y / L$ and equations (6.5). Let us consider the case $(Ra/Ra_c, C) = (2.5, 0.316)$, so that $u_x \sim 1.7\langle u_x \rangle_x$ and $L_0 \sim L$. Assuming $L \sim \beta^\lambda$, we determine λ by solving $\max(3\lambda, -2/3 + \lambda) = -\lambda_{RF}$. This equation always has a solution and we find

$$L \sim \beta^{-\lambda_{RF}/3} = \beta^{-0.31}, \quad (6.7)$$

where we used equation (4.13) for the value of λ_{RF} when $\beta \in [1.41 \times 10^6, 7.07 \times 10^6]$. In the strong zonal flow case, we proceed as follows. Setting $L_0 \sim \beta^{\lambda_0}$ we must solve $\max(2\lambda, -2/3) = -(\lambda_{RF} + \lambda_0) = -\lambda_S$, which does not always have a solution. We must require that $\lambda_S \leqslant 2/3$. Then

$$L \sim \beta^{-\lambda_S/2}. \quad (6.8)$$

Since $u_x \sim \langle u_x \rangle_x$, we may determine the radial length scale of u_x by the Rhines length scale associated with the zonal energy, $L_0 \sim \sqrt{U_Z/\beta}$, see (Rhines 1975). If the β-scaling of the zonal energy and the mean Reynolds force were given as in equation (4.13), we would obtain $\lambda_0 = -0.31$ and $L \sim \beta^{-0.31}$ again.

A numerical study of the convective length scale at $(Ra/Ra_c, C) = (2.5, 0.316)$ confirms that the β-scaling of convection has $\lambda \approx -1/3$. There are several ways to determine the length scale of the convective component u_y. Four possible definitions of the x-length scale are

$$\left(L_x^{(1)}, L_x^{(2)}, L_x^{(3)}, L_x^{(4)}\right)$$
$$= \left(\sqrt{\frac{\langle u_y^2 \rangle_{xy}}{\langle (\partial_x u_y)^2 \rangle_{xy}}}, \frac{\langle |u_y| \rangle_{xy}}{\langle |\partial_x u_y| \rangle_{xy}}, \sqrt{\left\langle \left|\frac{u_y}{\partial_{xx} u_y}\right|\right\rangle_{xy}}, \sqrt{\left\langle \left|\frac{\partial_x u_y}{\partial_{xxx} u_y}\right|\right\rangle_{xy}}\right). \quad (6.9)$$

The y-length scales $\left(L_y^{(1)}, L_y^{(2)}, L_y^{(3)}, L_y^{(4)}\right)$ of the convective flow may be defined in a similar way. For $\beta \in [1.41 \times 10^6, 7.07 \times 10^6]$, we find

$$\left(L_x^{(1)}, L_x^{(2)}, L_x^{(3)}, L_x^{(4)}\right) = (1.98\beta^{-0.32}, 2.03\beta^{-0.32}, 4.54\beta^{-0.32}, 4.41\beta^{-0.34}), \quad (6.10a)$$
$$\left(L_y^{(1)}, L_y^{(2)}, L_y^{(3)}, L_y^{(4)}\right) = (3.67\beta^{-0.33}, 3.57\beta^{-0.33}, 7.19\beta^{-0.33}, 5.38\beta^{-0.35}). \quad (6.10b)$$

For the length scales 1–3, the y-length scale is approximately twice the x-length scale whilst the length scale 4 results in almost equal x- and y-length scales. The scalings are all close to $\beta^{-1/3}$.

7. Conclusions

At moderate thermal driving, we have demonstrated β-scaling of several quantities. From these, we find that the Ekman dissipation remains important in the zonal flow equation, whilst bulk dissipation is the main source of energy depletion of the total flow. We have developed scaling arguments for the convective length scale and successfully compared this to the numerical simulations.

We have added to the understanding of the bursting phenomenon which takes the form of a relaxation oscillation. A short burst of convection enhances the zonal flow and rapidly changes the x-averaged temperature. Then follows a long period of relaxation in which the zonal flow and the temperature are smoothed out by diffusion. The next burst occurs when this smoothing has proceeded far enough to allow the unstable temperature gradient to overcome the stabilizing effect of the shear flow. The burst is shown to occur throughout the layer, but the convection-quiet times have more structure with thermal precursors and afterglows. Large-scale waves can be excited by the bursts, and their dispersion relation has been examined and shown to be consistent with thermal Rossby waves.

The presence of Ekman suction giving a boundary friction term can dramatically affect the solutions. The boundary friction influences the zonal flow, reducing the strength of the zonal flow, and making multi-jets much easier to find. In addition, we have explored how the behaviour is affected by varying the boundary friction parameter C. This is of interest because this parameter is non-constant in applications. In particular, we have shown that, at sufficiently large β, windows of C exist in which multi-jet solutions occur with the zonal flow containing more kinetic energy than the convection. Provided Ra/Ra_c is sufficiently large, these windows include realistic values of C when this quantity is in the form found in a simplified boundary curvature model. Applications of these results include experiments and enclosed planetary cores, where the outer surface is non-slip. For the gaseous planets, it is appropriate to assume a stress-free outer boundary, suggesting that the multi-jets observed outside the tangent cylinder in these planets and those found in experiments on rotating thermal convection are maintained by different mechanisms. However, our solutions along the lower boundary (small Ekman-layer strength) of the multi-jet windows demonstrate that only very weak viscous effects are required at the outer boundary to obtain more than two jets outside the tangent cylinder at low Ekman number.

REFERENCES

AUBERT, J., BRITO, D., NATAF, H.-C., CARDIN, P. & MASSON, J. P. 2001 A systematic experimental study of spherical shell convection in water and liquid gallium. *Phys. Earth Planet. Int.* **128**, 51–74.

AUBERT, J., GILLET, N. & CARDIN, P. 2003 Quasi-geostrophic models of convection in rotating spherical shells. *Geochem. Geophys. Geosyst.* **4**, 1052.

BRUMMELL, N. H. & HART, J. E. 1993 High Rayleigh number β-convection. *Geophys. Astrophys. Fluid Dyn.* **68**, 85–114.

Busse, F. H. 1970 Thermal instabilities in rapidly rotating systems. *J. Fluid Mech.* **44**, 441–460.

Busse, F. H. 1976 A simple model of convection in the Jovian atmosphere. *Icarus* **29**, 255–260.

Busse, F. H. 1994 Convection driven zonal flows and vortices in the major planets. *Chaos* **4**, 123–134.

Busse, F. H. 2002 Convection flows in rapidly rotating spheres. *Phys. Fluids* **14**, 1301–1314.

Busse, F. H. & Carrigan, C. R. 1976 Laboratory simulation of thermal convection in rotating planets and stars.*Science* **191**, 81–83.

Busse, F. H. & Hood, L. L. 1982 Differential rotation driven by convection in a rotating annulus. *Geophys. Astrophys. Fluid Dyn.* **21**, 59–74.

Cho, J. Y.-K. & Polvani, L. M. 1996 The morphogenesis of bands and zonal winds in the atmospheres on the giant outer planets. *Science* **273**, 335–337.

Christensen, U. R. 2001 Zonal flow driven by deep convection in the major planets. *Geophys. Res. Lett.* **28**, 2553–2556.

Christensen, U. R. 2002 Zonal flow driven by strongly supercritical convection in rotating spherical shells. *J. Fluid Mech.* **470**, 115–133.

Christensen, U. R., Aubert, J., Caroin, P. *et al.* 2001 A numerical dynamo benchmark. *Phys. Earth Planet. Inter.* **128**, 25–34.

Elliott, J. R. 2003 Numerical simulations of the solar convection zone. In *Stellar Astrophysical Fluid Dynamics*, (ed. M. J. Thompson & J. Christensen-Dalsgaard), pp. 315–329. Cambridge University Press.

Evonuk, M. & Glatzmaier, G. A. 2004 2D studies of various approximations used for modeling convection in giant planets. *Geophys. Astrophys. Fluid Dyn.* **98**, 241–255.

Fearn, D. R. 1998 Hydromagnetic flow in planetary cores. *Rep. Prog. Phys.* **61**, 175–235.

Gillet, N. & Jones, C. A. 2006 The quasi-geostrophic model for rapidly rotating spherical convection outside the tangent cylinder. *J. Fluid Mech.* **554**, 343–369.

Gilman, P. A. 1977 Nonlinear dynamics of Boussinesq convection in a deep rotating spherical shell. I. *Geophys. Astrophys. Fluid Dyn.* **8**, 93–135.

Gilman, P. A. 1978*a* Nonlinear dynamics of Boussinesq convection in a deep rotating spherical shell. II: Effects of temperature boundary conditions. *Geophys. Astrophys. Fluid Dyn.* **11**, 157–179.

Gilman, P. A. 1978*b* Nonlinear dynamics of Boussinesq convection in a deep rotating spherical shell. III: Effects of velocity boundary conditions. *Geophys. Astrophys. Fluid Dyn.* **11**, 181–203.

Greenspan, H. P. 1968 *The Theory of Rotating Fluids*. Cambridge University Press.

Grote, E. & Busse, F. H. 2001 Dynamics of convection and dynamos in rotating spherical fluid shells. *Fluid Dyn. Res.* **28**, 349–368.

Ingersoll, A. P. & Pollard, D. 1982 Motion in the interiors and atmospheres of Jupiter and Saturn: scale analysis, anelastic equations, barotropic stability criterion. *Icarus* **52**, 62–80.

Jones, C. A. 2003 Dynamos in planets. In *Stellar Astrophysical Fluid Dynamics* (ed. M. J. Thompson & J. Christensen-Dalsgaard), pp. 159–178. Cambridge University Press.

Jones, C. A., Rotvig, J. & Abdulrahman, A. 2003 Multiple jets and zonal flow on Jupiter. *Geophys. Res. Lett.* **30**, 1731.

Limaye, S. S. 1986 Jupiter: new estimates of the mean zonal flow at the cloud level. *Icarus* **65**, 335–352.

Manneville, J. B. & Olson, P. 1996 Banded convection in rotating fluid spheres and the circulation of the Jovian atmosphere.*Icarus* **122**, 242–250.

Morin, V. & Dormy, E. 2006 Dissipation mechanisms for convection in rapidly rotating spheres and the formation of banded structures. *Phys. Fluids* **18**, 068104.

Porco, C. C., West, R. A., McEwen, A. *et al.* 2003 Cassini imaging of Jupiter's atmosphere, satellites and rings. *Science* **299**, 1541–1547.

Rhines, P. B. 1975 Waves and turbulence on a beta-plane. *J. Fluid Mech.* **69**, 417–443.

Rotvig, J. 2006 Multiple zonal jets: thermal convection in rotating spherical shells compared to a set of quasi-geostrophic models. *Preprint*.

Rotvig, J. & Jones, C. A. 2002 Rotating convection-driven dynamos at low Ekman number. *Phys. Rev.* E **66**, 56308.

Russell, C. T., Yu, Z. J. & Kivelson, M. G. 2003 The rotation period of Jupiter. *Geophys. Res. Lett.* **28**, 1911–1912.

Starchenko, S. & Jones, C. A. 2002 Typical velocities and magnetic field strengths in planetary interiors. *Icarus* **157**, 426–435.

STEWARTSON, K. 1978 Waves in homogeneous fluids. In *Rotating Fluids in Geophysics* (P. H. Roberts & A. M. Soward). Academic.

TAYLOR, J. B. 1963 The magneto-hydrodynamics of a rotating fluid and the Earth's geodynamo problem. *Proc. R. Soc. Lond.* A **274**, 274–283.

TILGNER, A. & BUSSE, F. H. 1997 Finite-amplitude convection in rotating spherical fluid shells. *J. Fluid Mech.* **332**, 359–376.

TOOMRE, J. 2003 Bridges between helioseismology and models of convection zone dynamics. In *Stellar Astrophysical Fluid Dynamics* (ed. M. J. Thompson & J. Christensen-Dalsgaard), pp. 299–314. Cambridge University Press.

YANO, J.-I. 1998 Deep convection in the interior of major planets: a review. *Austral. J. Phys.* **51**, 875–889.

YANO, J.-I., TALAGRAND, O. & DROSSART, P. 2005 Deep two-dimensional turbulence: an idealized model for atmospheric jets of the giant outer planets. *Geophys. Astrophys. Fluid Dyn.* **99**, 137–150.

ZHANG, K. 1992 Spiralling columnar convection in rapidly rotating spherical fluid shells. *J. Fluid Mech.* **236**, 535–556.